

# RECONSTRUCTION OF MAGNETIC PLASMA BOUNDARY IN TOKAMAKS USING LOW DRIFT INTEGRATOR MEASUREMENTS AND STEADY STATE-SPACE MODELLING ON EDDY CURRENTS IN PASSIVE STRUCTURES

André Torres

75578

Laboratory rotation

APPlaUSE

November 2018

## 1 ISTTOK

ISTTOK (IST Tokamak) is a large aspect ratio tokamak with a circular cross-section located in IST, Lisbon. Perhaps the most distinguishable feature of ISTTOK is the capability of performing AC discharges, where the direction of the current is reversed upon reaching the saturation of the iron core [1]. Despite the small machine (major radius  $R = 0.46$  m, minor radius  $a = 0.085$  m) the parameters at the core are not very different from those at the edge of the plasma for larger machines, allowing the conduction of edge plasma studies. The fact that machine is small and reaches the operation conditions faster than larger machines, allows the conduction of a larger number of experiments and creates a prime environment to the development of new diagnostics and diagnostic techniques.

## 2 A nouvelle digital integration approach for the magnetic diagnostic

A good example of diagnostic development in ISTTOK is the new magnetic diagnostic. Previous implementations, in experiments worldwide, rely on analogical integrators. Nevertheless, this strategy has a shortcoming for long pulse durations – as the integration time grows, any small and systematic very low frequency or DC offset adds up to a large contribution, the drift. This led to a change of strategy in the development of the magnetic diagnostic for the W7-X stelerator [2], where instead of analogical integration, a digital integration with modulated input is used. The drift inducing DC offset added to the modulated signal is removed at demodulation. This approach was also followed for the ITER magnetic diagnostic [3] and ISTTOK [4] where the diagnostic and the techniques are kept under constant improvement.

While the drift can be isolated and removed from the magnetic data in post processing, that would make it impossible to use the magnetic diagnostic for real-time applications, such as position and plasma current control.

## 3 Active coils

ISTTOK has has 3 sets of active coils. Horizontal and vertical field coils and a primary circuit, installed later on Low Field Side (LFS). As seen in Figure 1, the vertical field is created by a quadrapole while horizontal field and primary coils are dipoles. Figure 2 shows the expected magnetic fields generated by this circuits on a poloidal cross-section.

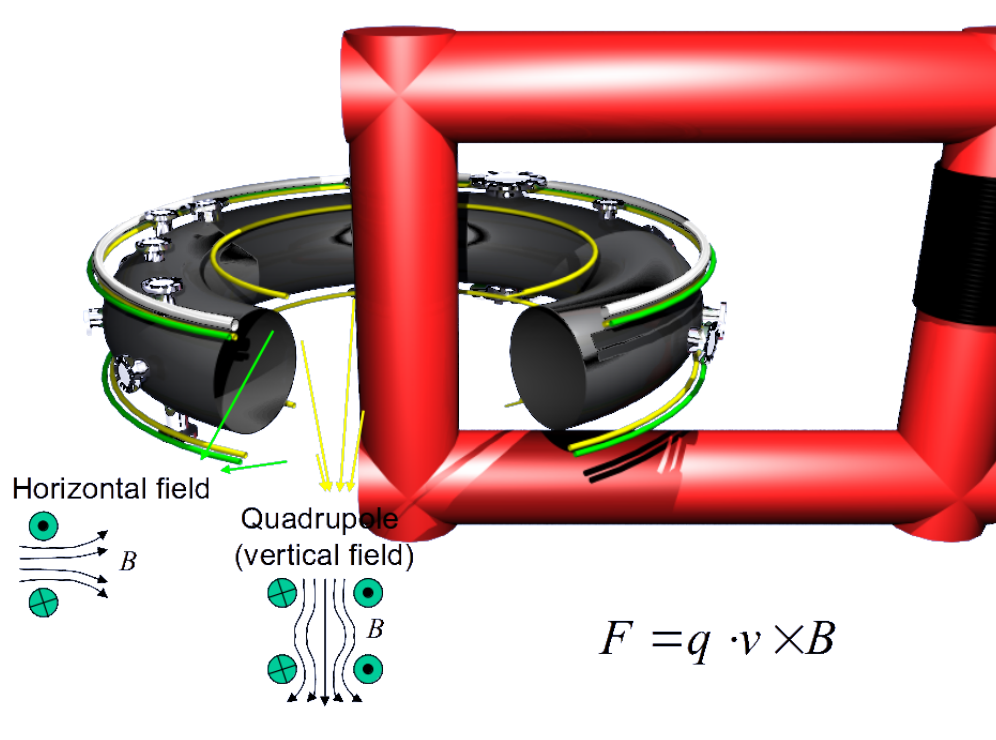


Figure 1: Model of ISTTOK with the active coils highlighted [5].

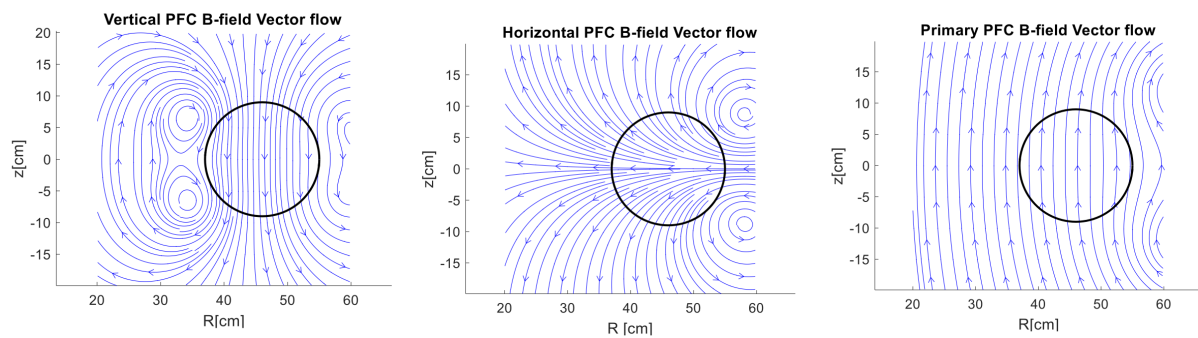


Figure 2: Magnetic field directions of the 3 circuits [6].

## 4 ISTTOK Magnetics Data

ISTTOK has a poloidal array of 12 Mirnov coils on access port number 3. Each of these probes has square  $12 \text{ mm}^2$  cross section and 50 windings and are numbered 1-12 starting from the lower equatorial plane on LFS with 30 deg separation.

The signals are acquired by the integrator boards described before. Since the real-time MARTe Generic Application Module (GAM) [7] is under development and to ensure consistency in the analysis, the drift removal (as well as polarity and unit conversion) is performed in post-processing by a set of functions in the git repositories [8, 9].

Figures 3 to 5 show the signals obtained in a plasma-less shot with only a Heaviside waveform in current supplied to the vertical field, horizontal field and primary circuits respectively.

It is visible that in the case of the horizontal field, the probes that are perpendicular to the field measure a very small flux, with the eddy current component being explicit. On the vertical field and primary circuits, there is not such a well defined difference between the top and bottom probes and the ones on LFS and HFS, that have signals in the same order of magnitude. This will be discussed further ahead as it has implications for the model implemented.

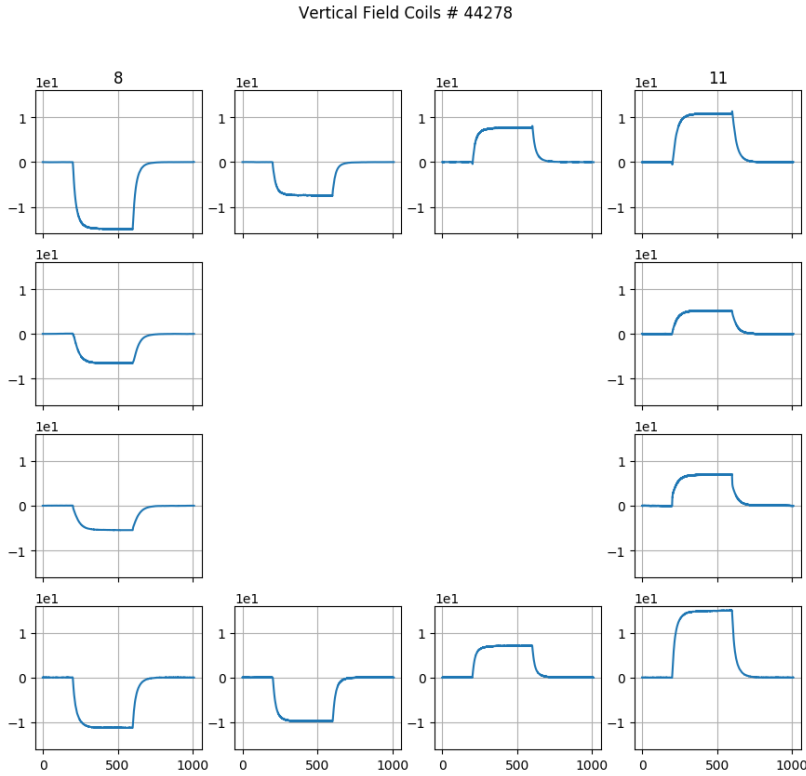


Figure 3: Signals from the array of 12 Mirnov probes in  $\mu\text{V s}$ . Plasma-less pulse #44278 with a current Heaviside on the vertical field coils circuit only.

Horizontal Field Coils # 44330

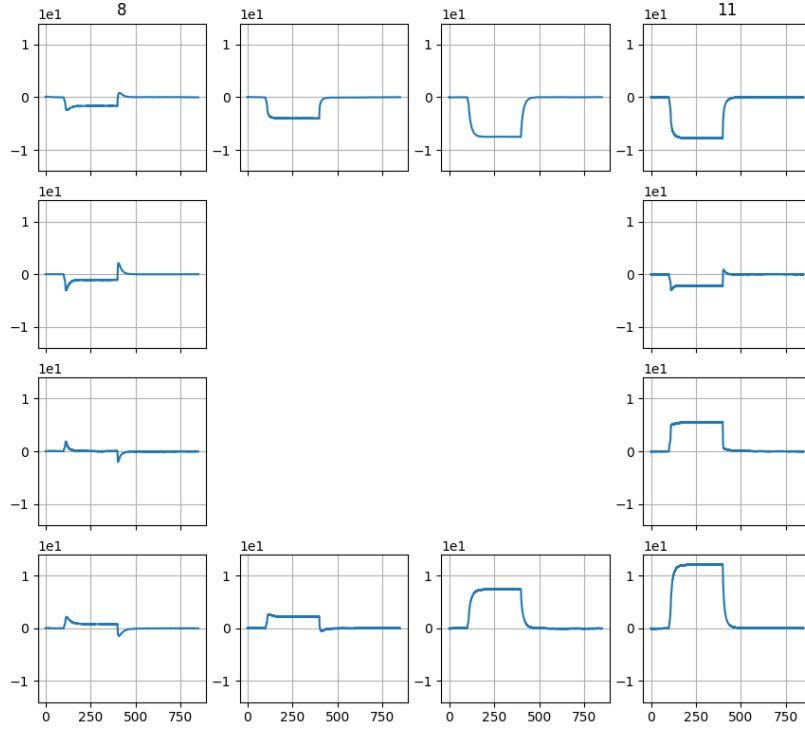


Figure 4: Signals from the array of 12 Mirnov probes in  $\mu\text{V}$  s. Plasma-less pulse #44330 with a current Heaviside on the horizontal field coils circuit only.

Primary Coils # 44501

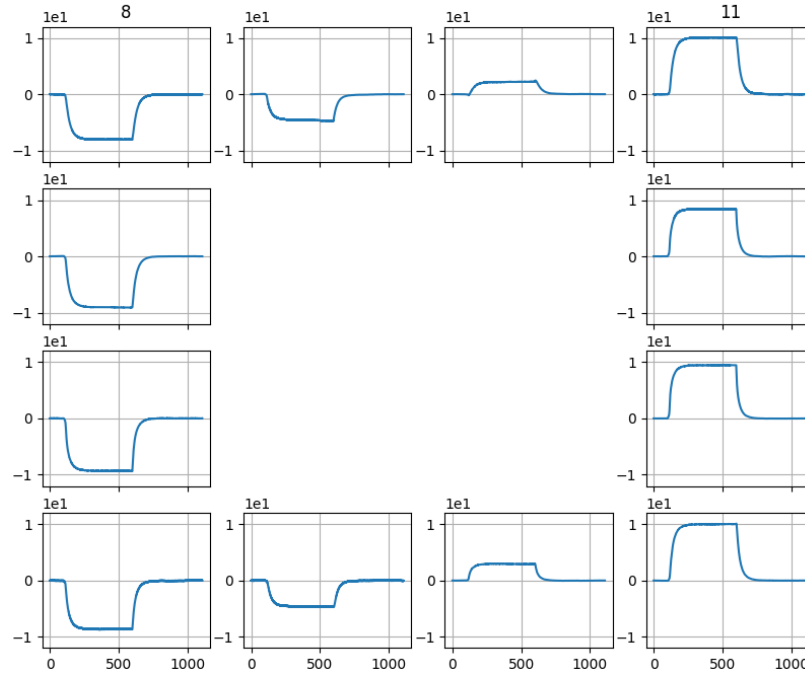


Figure 5: Signals from the array of 12 Mirnov probes in  $\mu\text{V}$  s. Plasma-less pulse #44501 with a current Heaviside on the primary circuit only.

## 5 Computation of the magnetic fields using the elliptic integrals

In order to apply the LTI model for the currents on the passive structures, one has to compute the magnetic field generated by the active coils. The active coils can be modeled as circular loops with a given radius (see Figure ??). The computation using the Biot-Savart law would require the employment of numerical methods. However, a quicker and accurate solution is possible, using the elliptic integrals as shown in [10]. For a current loop of radius  $a$  in the  $r, \theta$  plane the potential vector is given in spherical coordinates  $(r, \theta, \varphi)$  as

$$A_\varphi(r, \theta) = \frac{\mu_0 I a}{a\pi} \int_0^{2\pi} \frac{\cos\varphi' d\varphi'}{\sqrt{a^2 + r^2 - 2ar \sin\theta \cos\varphi'}} \quad (1)$$

$$= \frac{\mu_0}{4\pi} \frac{4Ia}{\sqrt{a^2 + r^2 + 2ar \sin\theta}} \left[ \frac{(2 - k^2)K(k^2) - 2E(k^2)}{k^2} \right], \quad (2)$$

where  $K$  and  $E$  are the elliptic integrals with argument

$$k^2 = \frac{4ar \sin\theta}{a^2 + r^2 + 2ar \sin\theta}. \quad (3)$$

With the auxiliary definitions  $\alpha^2 \equiv a^2 + r^2 - 2ar \sin\theta$ ,  $\beta^2 \equiv a^2 + r^2 + 2ar \sin\theta$ ,  $k \equiv 1 - \frac{\alpha^2}{\beta^2}$  and  $C \equiv \frac{\mu_0 I}{\pi}$ , the radial and vertical components of the field on the poloidal plane are

$$B_R = \frac{C}{2\alpha^2\beta R} [(a^2 + r^2)E(k^2) - \alpha^2 K(k^2)] \quad (4)$$

$$B_z = \frac{C}{2\alpha^2\beta} [(a^2 + r^2)E(k^2) + \alpha^2 K(k^2)] \quad (5)$$

## 6 Optimization of the Active Coils Positions

The first result would be to compute the magnetic flux on crossing the Mirnov coils. The results were odd – very far from the measurements of the Mirnov coils. While odd, this is not a surprising result. It is possible that the coils (particularly the vertical and horizontal field coils) are not in their assumed positions.

For this purpose, there was the need of figuring the actual or at least a virtual position of the active coils that generate a field similar to what is measured in the Mirnov coils.

The basic idea is to compare the field generated by the current used in the Heaviside with the flat top value of the signal on the Mirnov coils, taken as the mean of the stable region just before the current switches to 0 (see Figures 3 to 5). At first a least square minimization strategy was attempted but with 12 data points and at least 4 degrees of freedom (DoF) (8 for the vertical field coils), a manual fitting was preferred, using an interactive script that allows us to see the effect each change in position and current has in real time.

In the end, 3 optimization criteria were defined and applied for the 3 circuits: optimization 1 varying only the  $R, z$  positions of the coils; optimization 2 allowing also a gain factor on the current (scale factor); optimization 3 dividing this gain factor in the components of vertical and radial field. There are no real physics behind optimization 3 and therefore its results should be ‘taken with a grain of salt’ and will not have continuation in the application of the model. However, if the results are deemed consistently better, they could indicate an issue with the Mirnov array (miscalibration or misalignment). Specifically for the results presented here, horizontal flux was amplified and the vertical flux attenuated, given that the high signal on the coils that should measure very little vertical field was detected in Figures 3 and 5.

Figures 6 to 8 show the positions and expected fluxes crossing the Mirnov coils for the nominal and 3 optimized positions, discriminated in Tables 1 to 3.

In general, the results show more agreement across optimization than with the nominal positions. While very small displacements from the nominal positions are seen for the primary windings, the results for older vertical and horizontal field coils, bundled together on LFS, are highly suggestive of a major and real displacement.

While measurements are difficult on LFS and almost impossible on HFS, comparing the locations with an actual photo (Figure 9) seem to corroborate the preliminary results.

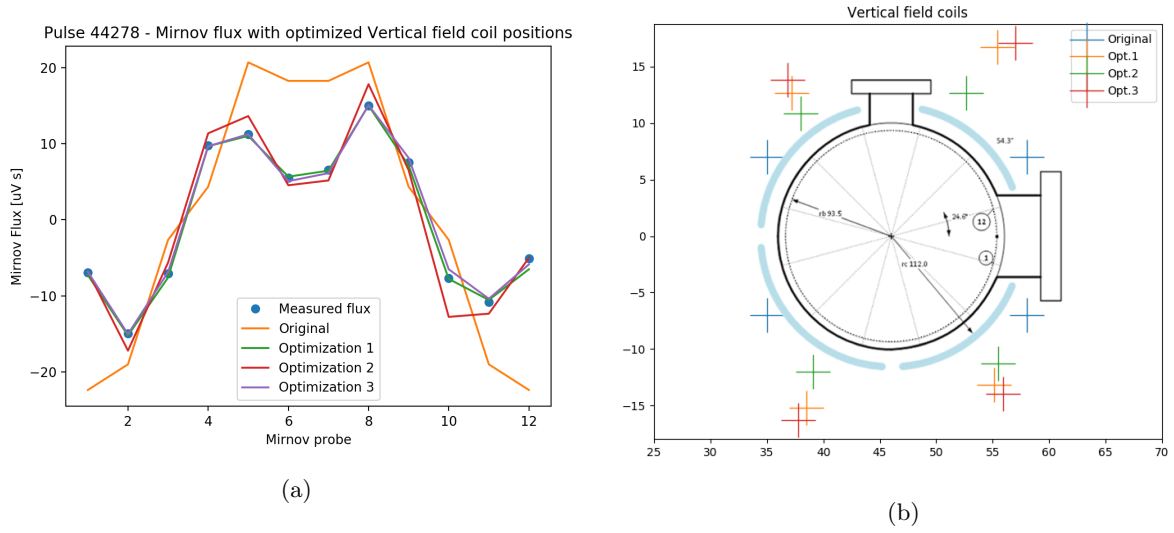


Figure 6: Result of the optimizations of the vertical field coils positions as in Table 1. Optimization 1 corresponds to an optimization in which only the coil positions are changed whereas on optimizations 2 and 3 the current and a gain factors on the magnetic field components, respectively, are added.

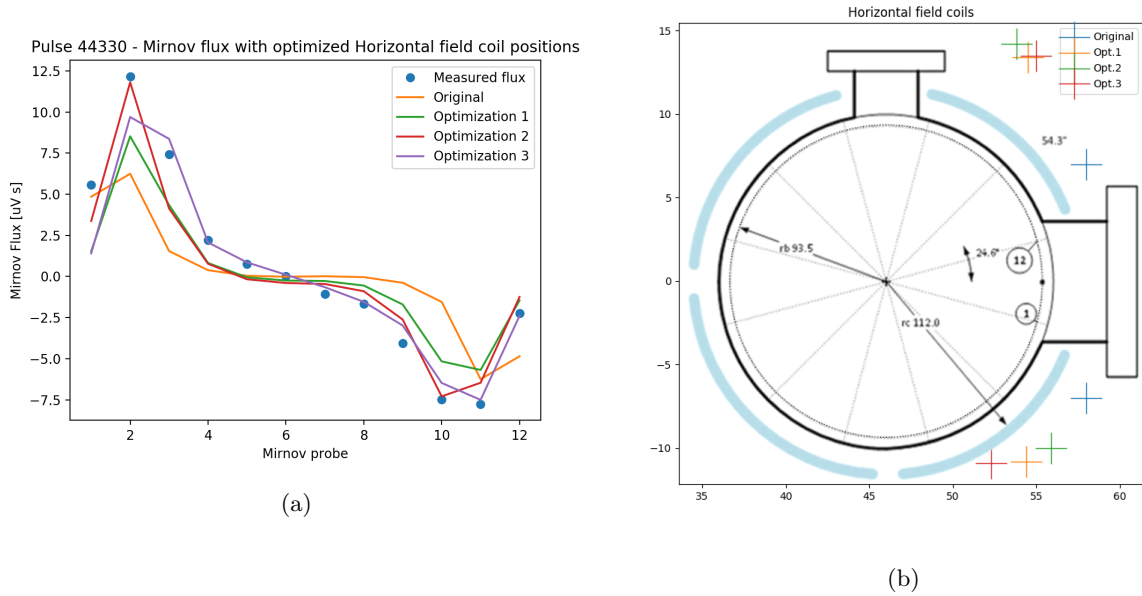


Figure 7: Result of the optimizations of the horizontal field coils positions as in table 2. Optimization 1 corresponds to an optimization in which only the coil positions are changed whereas on optimizations 2 and 3 the current and a gain factors on the magnetic field components, respectively, are added.

Optim.	R [cm]	Z [cm]	Notes
Nominal	58	-7	5 windings
	58	7	
	35	-7	
	35	7	
1	55.1	-13.2	
	55.4	16.7	
	38.5	-15.2	
	37.2	12.7	
2	55.47	-11.25	0.83 I gain
	52.64	12.68	
	39.05	-12.04	
	38.03	10.89	
3	55.9	-14	1.6 $B_R$ gain
	57.0	17.1	
	37.8	-16.3	0.8 $B_Z$ gain
	36.8	13.8	

Table 1: Nominal and optimized positions for the vertical field coils.

Optim.	R [cm]	Z [cm]	Notes
Nominal	58	-7	4 windings
	58	7	
1	54.4	-10.8	
	54.5	13.4	
2	55.9	-10.0	1.324 I gain
	58.8	14.6	
3	52.3	-10.9	1.6 $B_R$ gain
	55.0	13.5	0.8 $B_Z$ gain
			0.91 I gain

Table 2: Nominal and optimized positions for the horizontal field coils.

Optim.	R [cm]	Z [cm]	Notes
Nominal	62	-13	14 windings
	62	13	
1	61.5	-14.4	
	61.5	14.5	
2	60.6	-14.1	0.842 I gain
	60.6	13.9	
3	61.8	-13.9	1.6 $B_R$ gain
	62.2	15.2	0.8 $B_Z$ gain

Table 3: Nominal and optimized positions for the primary coils.

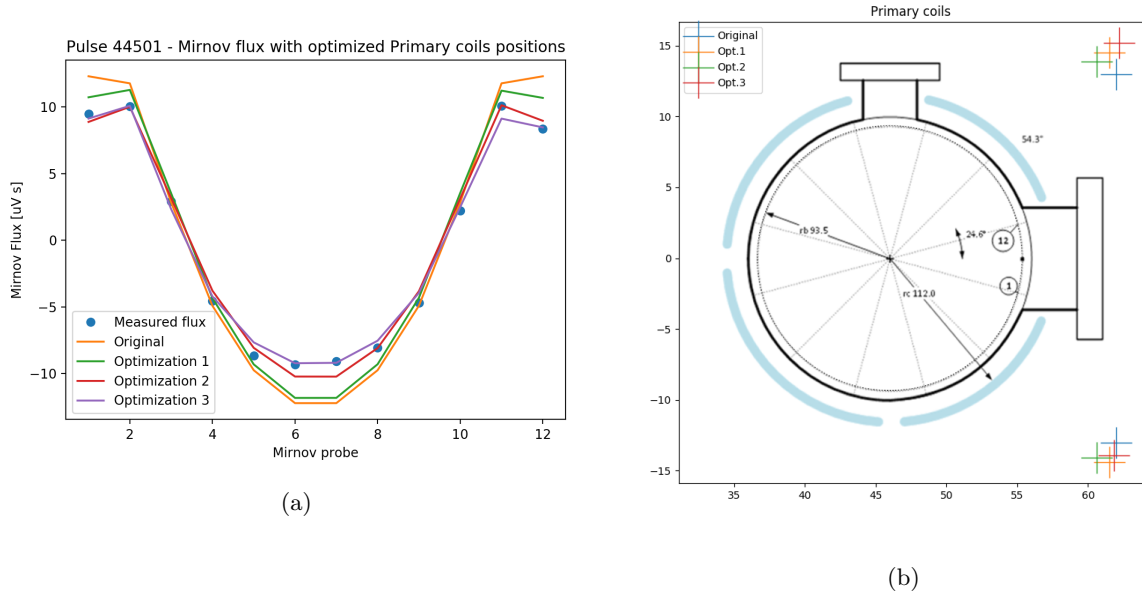


Figure 8: Result of the optimizations of the primary coils positions as in table 3. Optimization 1 corresponds to an optimization in which only the coil positions are changed whereas on optimizations 2 and 3 the current and a gain factors on the magnetic field components, respectively, are added.

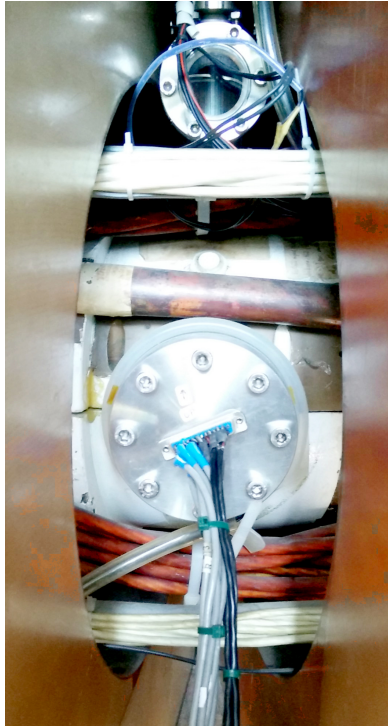


Figure 9: Photography of the access port 3 of ISTTOK. Mirnov connections on the equatorial port, primary coils in white and horizontal and vertical in orange.



## 7 Application of the filamentary currents state-space model

In order to model both the direct influence of the active coils on the Mirnov coils as well as the indirect contribution through eddy currents on the copper shell, a Linear Time-Invariant (LTI) model was implemented, based on a more complete description published earlier this year [11].

This model is based on the computation of the mutual inductances between the currents on the active coils, or sources,  $i_c$  and the passive structures filaments current  $i_c$ ,  $M_{cs}$ ; and among the filaments  $M_{cc}$ ; and the resistance of such filaments  $R_c$ .

The LTI model is then defined as:

$$\begin{aligned}\dot{\Psi}_c &= -R_c M_{cc}^{-1} \Psi_c + R_c M_{cc}^{-1} M_{cs} i_s \\ i_c &= M_{cc}^{-1} \Psi_c - M_{cc}^{-1} M_{cs} i_s\end{aligned}$$

$$\begin{aligned}\dot{\Psi}_c &= A \Psi_c + B i_s \\ i_c &= C \Psi_c + D i_s\end{aligned}$$

where  $R_c$  is a diagonal matrix and  $\Psi_c$  is the state variable, the flux on the passive structures.

Axial symmetry was assumed and the passive structure filaments were defined as toroidal loops with copper resistivity  $\rho = 1.68 \cdot 10^{-8} \Omega\text{m}^{-1}$  and a radius corresponding to half of the copper shell thickness  $a = 10$  mm. The self inductance (main diagonal of  $M_{cc}$ ) was determined as

$$L_c = \mu_0 R (\ln(8R/a)) - 2 + Y/2$$

with  $Y = 0.5$  for a homogeneous current across the loop with radius  $R$  [12].

Mutual inductances between loops was determined as

$$L_{i,j} = 2\pi R A_\varphi(R, z) .$$

As in the previous section, here the high number of degrees of freedom is problematic – number of filaments, position, size. The copper shell however imposes some boundaries as the poloidal cross section is divided in 4 sections: [20, 70], [110, 175], [180, 265], [275, 340] °.

Once again, an interactive script was developed [9]. The algorithm allows the adjustment of the angle of each of the individual filaments individually while observing its effect on the 3 closest Mirnov coils. The script is also prepared to use the optimizations of the active coils positions.

The results presented here are for a horizontal field coils pulse (44330) using the optimization 2 (with current gain) for the active coils positions. The reason for choosing the horizontal field Heaviside versus the primary is that in the horizontal field, the eddy current contributions are more visible and with the optimized positions (regardless of being actual or virtual positions), the agreement with the measurements for the steady part is also very good. While the model can predict a flux on the Mirnov coils with a reasonable degree of agreement with the measurements (see Figure 10), when this combination of filaments is used on the primary or vertical field pulses, the results are not that good anymore (see Figure 11). This probably means that improvements on the model are needed, rather than proceeding with a manual optimizations, as discussed in the next section.

Another somehow unexpected result is that the currents seem to be in the same direction, see Figure 12.

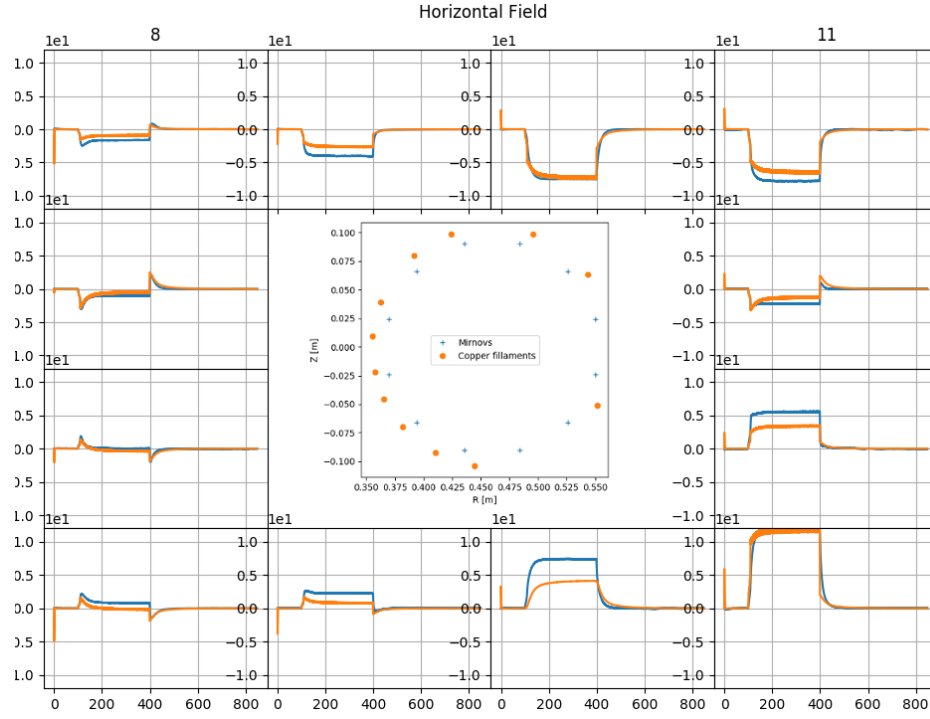


Figure 10: Optimization of the positions of 12 filaments in the copper shell (center) and the response on the 12 Mirnov coils.

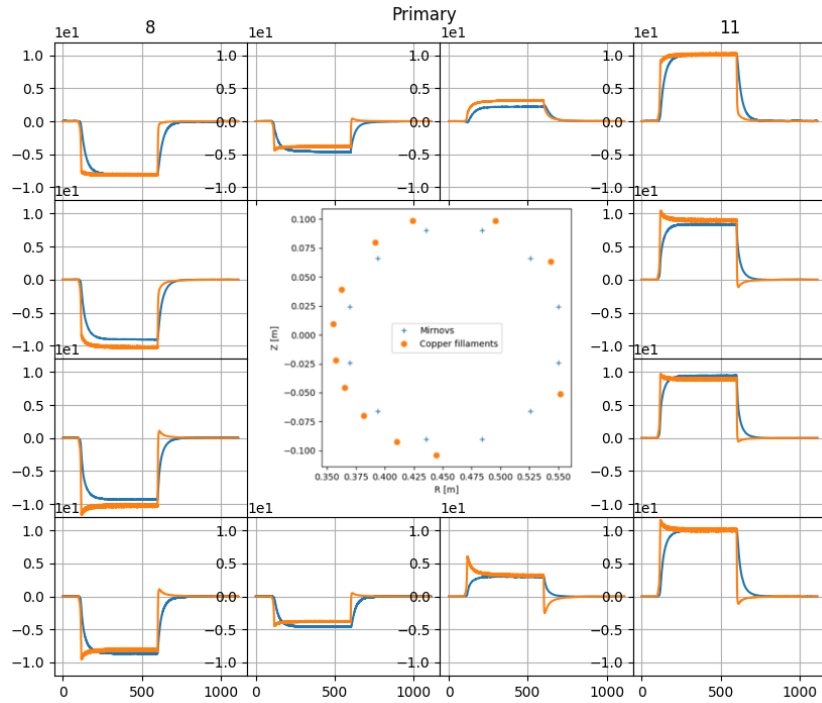


Figure 11: Optimization of the positions of 12 filaments in the copper shell (center) and the response on the 12 Mirnov coils using a pulse with current on the primary coils.

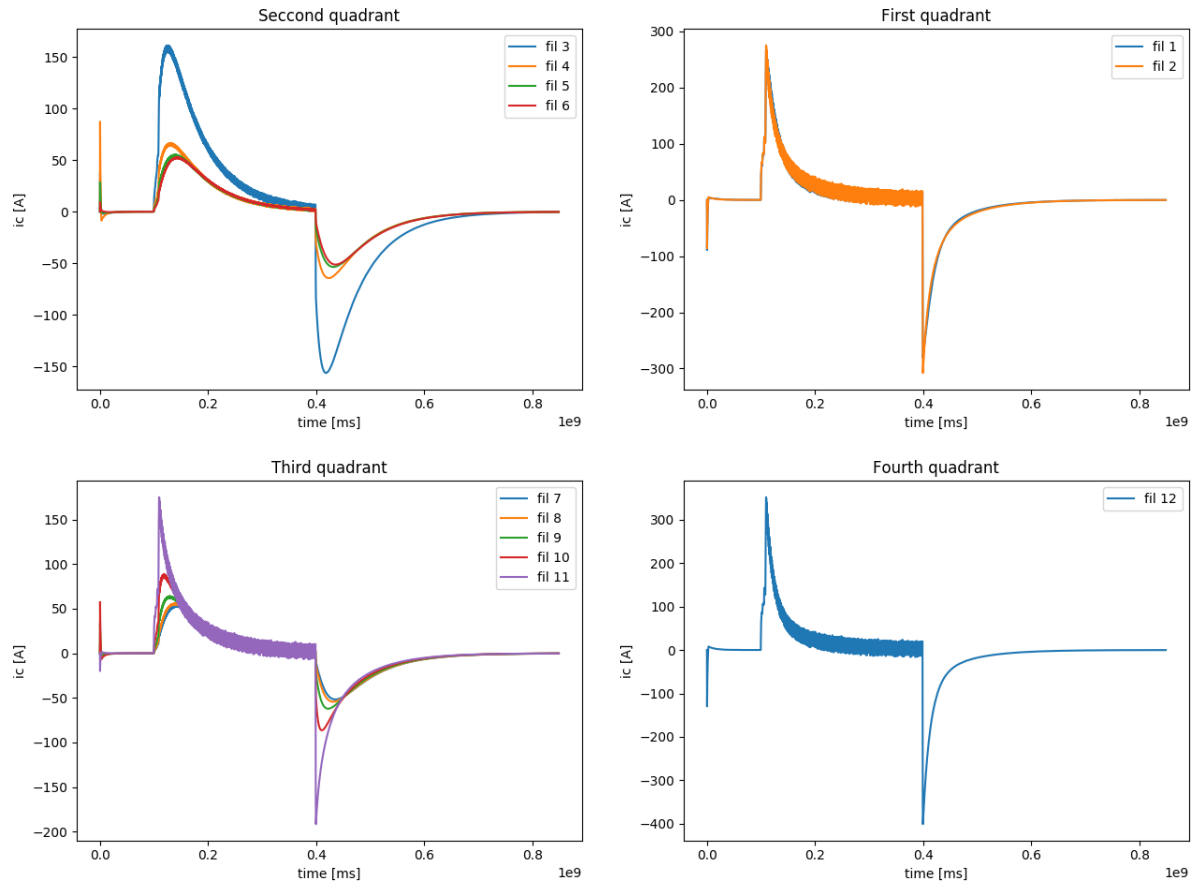


Figure 12: Current on the filaments, separated in quadrants.

## 8 Conclusions and further work

While this work did not reach good enough results to have a reliable reconstruction of the plasma boundary, it provided surprising and important conclusions and opens several paths for proceeding in further work.

The LTI model was successfully applied, even though it did not reach successful results. In fact, one of the reasons for this might lie in one key assumption for this model – the passive structure on ISTTOK that was modeled, is not axysymmetrical. It is divided in several toroidal sections. A LTI model is a valid approach but the computation and geometry of the filaments have to account for this geometry of the copper shell.

Probably the most relevant results are the optimizations of the coils positions. It is probable that the nominal positions are wrong and this have implications for several studies carried out in ISTTOK. For this reason, it is advisable that some possible measurements are carried out (absolute or relative) to reduce the number of degrees of freedom and re-apply the optimization algorithms.

An important correction for the two parts of the work is to consider the propagation of the magnetic field in the iron core of the tokamak. This could explain why the results on HFS are more difficult to fit and including its contribution lead to a better optimization of the coil positions.

Another possible source of errors comes from the Mirnov coils themselves. An external calibration would be beneficial in order to determine the effective area of each coil. A corrective factor can then be implemented in the MARTE GAM performing the integration.

## References

- [1] H. Fernandes *et al.*, “20 years of isttok tokamak scientific activity,” [www-naweb.iaea.org/napc/physics/FEC/FEC2012/papers/651\\_OVP08.pdf](http://www-naweb.iaea.org/napc/physics/FEC/FEC2012/papers/651_OVP08.pdf), 2012, accessed 17/09/2018.
- [2] A. Werner, “W7-X magnetic diagnostics: Performance of the digital integrator,” *Review of Scientific Instruments*, vol. 77, no. 10, p. 10E307, 2006. [Online]. Available: <http://dx.doi.org/10.1063/1.2220073>
- [3] A. J. N. Batista, “F4E prototype of a chopper digital integrator for the ITER magnetics,” in *SOFT*, 2016.
- [4] D. Corona, N. Cruz, J. J. E. Herrera, H. Figueiredo, B. B. Carvalho, I. S. Carvalho, H. Alves, and H. Fernandes, “Design and Simulation of ISTTOK Real-Time Magnetic Multiple-Input Multiple-Output Control,” *IEEE Transactions on Plasma Science*, vol. 46, no. 7, pp. 2362–2369, 2018.
- [5] H. Fernandes, “Isttok machine description - course on tokamak engineering, diagnostics and operation,” 2018.
- [6] D. Corona, “Plasma control - course on tokamak engineering, diagnostics and operation,” 2018.
- [7] A. C. Neto, F. Sartori, F. Piccolo, R. Vitelli, G. D. Tommasi, L. Zabeo, A. Barbalace, H. Fernandes, D. F. Valcarcel, and A. J. N. Batista, “Marte: A multiplatform real-time framework,” *IEEE Transactions on Nuclear Science*, vol. 57, no. 2, pp. 479–486, April 2010.
- [8] A. Torres, “Isttok,” <https://github.com/andregtorres/ISTTOK>, 2018.
- [9] B. Carvalho and A. Torres, “isttok-python,” <https://github.com/andregtorres/isttok-python>, 2018.
- [10] J. Simpson, J. Lane, C. Immer, and R. Youngquist, “Simple Analytic Expressions for the Magnetic Field of a Circular Current Loop,” *NASA Technical Report*, pp. 1–3, 2001. [Online]. Available: <http://www.csa.com/partners/viewrecord.php?requester=gs{&}collection=TRD{&}recid=N0217988AH>
- [11] A. Cenedese, P. Bettini, and M. Bonotto, “Model-Based Approach for Magnetic Reconstruction in Axisymmetric Nuclear Fusion Machines,” *IEEE Transactions on Plasma Science*, 2018.
- [12] R. Dengler, “Self inductance of a wire loop as a curve integral,” no. January, 2012. [Online]. Available: <http://arxiv.org/abs/1204.1486>